

**Experimental measurement of wrinkle formation
during draping of non-crimp fabric**

SE Arnold, MPF Sutcliffe*, WLA Oram

Cambridge University Engineering Department, Trumpington Street,
Cambridge, CB2 1PZ, U.K.

Abstract

A rig and image analysis methodology is described to characterise wrinkle formation during draping of non-crimp fabrics. The circular fabric blank is draped over a male hemispherical mould, partly constrained by a circular clamping ring around the periphery of the blank. The three-dimensional shape of the fabric is derived from a shape-from-focus analysis of a stack of photographs of the deformed blank. Wrinkles are identified from the deviation of the shape from a smoothed shape. Wrinkle formation is strongly dependent on the fabric architecture and increases progressively with increased punch displacement. Triaxial fabrics have the highest wrinkle amplitude, unidirectional and 0/90° biaxial fabrics the lowest amplitude. The clamping force reduces the wrinkling for some fabrics but, for the maximum force applied, is not effective at eliminating wrinkling.

Keywords: Carbon fibre (A), Fabrics/textiles (A), Defects (B), Preforming (E), Wrinkling

* Email: mpfs@eng.cam.ac.uk, Tel: +44 1223 332996, Fax: +44 1223 332662

1 Introduction

Non crimp fabrics (NCF) are attractive in a range of composite applications because of their good mechanical performance, handling characteristics, and because multi-axial tows can be stitched together to form a heavier-weight fabric [1, 2]. Typically the dry fabric will be pre-formed at low pressure, perhaps using a blank holder to control the fabric movement, and then resin will be injected in a resin transfer moulding stage. Such a process route lends itself to automation with applications, for example, in the aerospace and automotive industries [2-4]. At present the selection of an appropriate fabric type which will work for a given geometry and draping process relies on experience and testing. Although simulations have been developed to model draping, development of defects and wrinkles remains an area of concern [5, 6].

Drape modelling for woven fabrics has become reasonably mature, with a range of models of varying complexity used to predict the deformation behaviour [7]. The simplest kinematic pin-jointed net model can give a reasonable prediction of in-plane shear deformation [5]. Wrinkling is commonly supposed to occur when the tows 'lock-up' as shear in the fabric reaches some critical value [8]. However this over-simplifies the picture when modelling the effect of membrane stresses and out-of-plane wrinkle deformations, with more sophisticated models and associated experiments highlighting the importance of the in-plane and bending components of the fabric forces in determining wrinkling [8-10]. Once these factors are included, such drape models give a reasonable prediction of wrinkling behaviour of woven fabrics, as well as the associated shear deformation [11].

The difference in tow architecture and the introduction of stitches in NCFs means that a simple pin-jointed network approach for drape modelling is no longer able to predict the deformation mechanism and wrinkle development accurately. Instead more sophisticated material models are needed to capture the drape behaviour [1, 12-14]. Both experiments and simulations highlight the effect of blank holder forces on wrinkle deformation [6, 13]. While these simulations are encouraging, particularly in terms of the shear deformation modelling, the comparison and validation of models of wrinkling with experiments is somewhat limited, with ad hoc comparisons of the pattern and wrinkle height for a given geometry. Such models would benefit from a richer study of the way that such wrinkles develop, including more data on the location and geometry of the wrinkles, to improve the confidence in the quantitative predictions.

It appears that a hindrance to understanding of wrinkle development is a relative sparsity of good data characterising these features, particularly for NCFs. Al-gaadi et al. [15] used a laser set-up to re-construct the profile of draped cotton fabrics, characterising the wrinkles formed by the amplitude of deviations of the shape from a mean value. Lee et al. [6] measured wrinkling in a formed NCF fabric via the effect such wrinkles have on scattering of laser light. Although the information gained about the wrinkle geometry is somewhat limited in this approach, the method nevertheless provides a quantitative way of demonstrating the reduction of wrinkling with increased blank holder force. Domskienė et al [16] described a more rudimentary approach, again using the effect of wrinkles on scattering of light, to quantify wrinkle formation. More recently Christ et al. [17] used a laser triangulation sensor and camera set-up to measure the shape of the draped fabric, in a system which is available commercially by Textechno. Ouagne et al. [18] measured tow buckling when draping a plain weave flax over a tetrahedron using a camera system. Finally three dimensional (3D) shape reconstruction using two cameras is now a well-established technique which has been applied to textile deformation (see for example [19]) and in principle this could also be used to measure wrinkles. So, while there is a range of techniques which can adequately measure wrinkling in fabrics, it appears that there is a significant overhead associated with adopting any of these measurement techniques, limiting their more widespread use.

The aim of the research is to develop a simple and repeatable way to measure the formation of wrinkling defects during draping of fabric. The method is used to investigate wrinkle formation during pre-forming of non crimp fabrics, where the wide range of tow orientations and stitch patterns available means that a simple drape assessment tool is critical to effective process development. As well as providing a simple tool to identify which fabrics would be appropriate for a given application, the development of a more complete method for characterising wrinkle evolution can provide insights into the key elements needed in a model for wrinkle development and a comprehensive set of validation data for such a model.

2 Experimental method

Figure 1 shows a schematic of the experimental rig used to investigate wrinkle formation. In order to be able to view wrinkle evolution during draping, initially-flat fabric was formed over a male-only hemispherical mould, in conjunction with a blank holder clamping ring. It is supposed that the mode of wrinkle formation in this process would also be typical of a matched mould

process, albeit in the latter case that the constraint of the two moulds could limit the extent of wrinkle formation. An imaging methodology was developed to characterise the evolution of wrinkles, based on a 'shape-from-focus' method, chosen because of its relatively simplicity. In this approach a 'z-stack' of images is used to build up the 3D geometry. Details of the materials, mechanical design, draping procedure and image analysis methodology are given below.

2.1 Materials

A range of non-crimp carbon fabrics was tested as detailed in Table 1, comprising a unidirectional fabric, $\pm 45^\circ$, $\pm 60^\circ$ and $0/90^\circ$ biaxial fabrics and two triaxial fabrics of differing weights, termed here light and heavy triaxial. The $\pm 60^\circ$ biaxial fabric contained powder binder. In all cases the stitching direction runs in the 0° direction so that all the fabrics are symmetrical about this stitching direction but do not have any other symmetry axes. Manufacturer's data sheets are included in a data repository [20].

2.2 Draping rig

The draping rig is based on the testing rig described by Christ et al [17], in which fabric is formed over a convex axisymmetric male tool, held in place by a transparent clamping ring. The realisation of this concept in our study is illustrated in Fig. 1. The design is built around a photographic enlarger head which provides the basic frame and mechanism for vertical travel. The male punch, manufactured out of modelling board, has a 75 mm radius hemispherical shape. The circular fabric blank of diameter 380 mm is held between a supporting ring, again made of modelling board, and a transparent perspex clamping ring. The inner and outer diameters of the clamping ring are 287 and 383 mm. Pressure is applied to the fabric through the clamping ring via a relatively stiff aluminium weight ring sitting on top of the clamping ring, on which deadweight loads are distributed at four locations around the ring, up to a total maximum weight of 8 kg. To this is added the 1.4 kg weight of the clamping and weight rings, even in the absence of additional weights. A simple beam bending calculation predicts that the deflections associated with uneven loading through the weight ring would be 20 μm at the maximum clamping load of 8 kg, assuming that the weights are reacted by point loads from the fabric mid-way between the weight locations. The actual deformations will be significantly less than this, since the reaction from the fabric will be more evenly distributed. This calculation

indicates that such deflections will not lead to uneven loading, as such small deflections can be taken up by the compliance of the fabric.

Further modifications to the enlarger head include insertion of a load cell between the frame and the punch, and mounting of a stepper motor and gearbox on the side of the enlarger head, connected to the rack and pinion mechanism on the enlarger head. The stepper motor is controlled through a custom-built motor controller unit by Labview software, driven by a laptop PC through an NI USB-6009 interface. The speed of the punch is controlled via a software loop in Labview. Although this method of controlling the forming speed is not very accurate, as it depends on the PC clock speed, this is not considered to be a critical factor for the dry fabrics being tested. Gearbox backlash and flexure of the rig limit the accuracy of the displacement control, with an error of approximately ± 0.5 mm. The NI interface device is also used to log the signal from the load cell, via a strain bridge amplifier. Digital filtering is used to remove noise in the logged signal, applying a low-pass Butterworth filter using a Matlab programme. Calibration of the load cell is performed using deadweight loading. The full set of load data for the different materials has been deposited in the online data depository.

2.3 Imaging

In the testing rig described by Christ et al [17], two cameras and a laser triangulation sensor were used to characterise the shape of the draped fabric. Our arrangement uses a single SLR camera (Canon EOS 1200D) with a 18 MegaPixel CMOS sensor and an 18-55 mm lens, mounted centrally under the deforming blank. The camera is used to image the fabric as it is progressively deformed. An LED light ring attached to the camera provides even lighting to the fabric. Tethering software (Helicon Remote) is used to control the camera via the laptop PC. This software automates the collection of a z-stack of images at a given stage in the deformation process. During this acquisition phase the focus position of the camera is varied within the stack by incrementing the focus motor position of the camera in typically 20 small steps to span the minimum and maximum distances to the fabric. The tethering software also gives accurate control of exposure and aperture size. Camera settings were varied depending on the exact lighting, but typical values of a 0.25 s exposure time, 3.5f aperture and ISO 100 were used.

2.4 Drape procedure

An Olfa cutter was used to cut out the fabric blank of diameter 380 mm around a circular sheet-steel template. A copper wire was laid across the blank holder, under tension, to support the blank and prevent it sagging before the clamping ring had been positioned and loaded up to hold the blank in place. The fabric blank was then added, and aligned visually such that the 0° weft fibres ran left to right in photos. Appropriate weights were then added to the clamping ring before the copper wire was removed. To simplify the testing procedure and ensure repeatability, a graphical user interface was developed in Labview to control the rig and handle the limit switches incorporated into the design control. The bottom punch was first brought down level with the top of the supporting ring; this location is used as a datum for the punch displacement. The program was then run to move the punch downwards at a speed of 1.5 mm/s, pausing after punch displacements of 20, 40, 50, 60, 70, and 75 mm for imaging of the deformed fabric. Figure 2 shows a typical photograph of the heavy triaxial fabric after the full punch displacement of 75 mm, showing the severe wrinkling present in this test.

2.5 Image Analysis

The idea of the shape-from-focus (SFF) technique used to reconstruct the 3D fabric shape is to select, for a given pixel in the image, the image from a z-stack of images which has the best degree of focus. By collating information from all pixels in an image, both the height information for each pixel and a sharp in-focus image at all locations can be reconstructed. The method has been applied successfully to microscopic images which typically have a relatively narrow depth of field [21], but has not been so widely used with conventional camera set-ups [22]. The effectiveness of the method depends on the imaging details, including the presence of features which can help identify the degree of focus. Details of the algorithm, including different measures of the depth of focus, affect the reliability and effectiveness of the method Pertuz [22, 23].

The Matlab algorithm developed in our study uses the basic concept of SFF, as detailed for example by Pertuz et al. [22, 24], but has been modified very substantially as described below to optimise for quality and robustness given the specific features of the images obtained in this study. In particular, the stitching in five of the six NCF fabrics provided high-contrast features to measure focus, see Fig. 2. However the SFF method needed to be tuned to accommodate the

spacing and intermittent nature of the stitching patterns. The exception was the unidirectional fabric, which used carbon stitching. Here the tow architecture provided less satisfactory but workable features. Although Pertuz et al. recommend wavelet operators for macro images [22, 23], the Laplacian operator was chosen on account of its much faster operation. Firstly the Laplacian measure of focus measure was calculated for all the pixels in the z-stack. This data was then smoothed within each image in the lateral dimensions using a square averaging filter of width equal to 18 pixels. Images were then downsampled by a factor of 4 in the horizontal and vertical directions to make the calculations more manageable. There is insignificant loss of information associated with this downsampling, given the prior smoothing operation. A smoothing filter was applied in the out-of-plane z direction with an in-built Matlab smoothing algorithm, using a robust least squares quadratic fit with a span of 10 points. The z position of maximum focus was then found for each pixel. To refine this estimate of the position of maximum focus, a quadratic interpolation of the measure of focus as a function of z position was used, applied to the location of maximum focus measure and two points either side. To eliminate noise in the resulting height data, a median filter (with a span of 20 pixels) and then a 3D fitting function (matlab function *gridfit* [25], used with a 'smoothness' of 50 pixels) were applied, resulting in a smoothed height data set interpolated onto a regular grid of spacing 1 mm. The region of interest in the image containing the part of the blank visible through the blank-holder supporting ring was identified using a matlab function *imfindcircles*, based on circular Hough transforms [26]. Scaling of the in-plane dimensions was performed using the known diameter of the support ring, while the out-of-plane dimension was linearly scaled from the z-stack locations using the known rim and peak heights of the deformed blank. A small correction associated with errors in the planarity of the focus plane was made using a correction function extracted from measurements on a flat steel sheet imaged at the position of the undeformed blank. Further details of the Matlab implementation of the imaging tools described above are given in [27]. Figures 3 (a) and (b) illustrate the results of this analysis for the light triaxial fabric at a punch deformation of 75 mm, showing in (a) the height data extracted from the stack, and in (b) the fitted height data interpolated onto the regular grid. In each plot the colour corresponds to the z position of each point on the fabric. The parameters used to perform the smoothing and fitting analysis have been chosen to ensure that the smoothed data in (b) reproduces the essential features seen in the raw data of (a), but with minor perturbations and noise in the signal effectively eliminated.

The analysis procedure was validated by imaging and analysing a piece of white card, formed into a cone of the same height and diameter as the deformed blank, and sprayed with black paint to create a speckle pattern. The shape-from-focus method itself has been well documented [21, 22], and the raw height images of Fig. 3(a) confirm that the fabric images used have an appropriate set of features to apply this methodology and derive a smooth surface map. Hence the calibration setup was chosen especially to validate the height extraction from the images. Details of the calibration are included in the Appendix.

2.6 Wrinkle analysis

To examine the amplitude and position of wrinkling, the deviation of the deformed fabric from an idealised shape needs to be found. To find the mean shape of the fabric (i.e. neglecting any wrinkling) the matlab *gridfit* algorithm was again used, but now with a very large smoothing parameter of 1000, so as to form a very smooth fit to the shape. The wrinkle height is then given by the difference between the total shape and the smoothed shape. This procedure is further illustrated in Fig. 3 for the light triaxial fabric considered above, comparing the total shape in (b), the smoothed shape in (c) and the resulting wrinkle shape, being the difference between these, in (d). Note that the large smoothing parameter chosen for (c) ensures that no small scale wrinkle features are retained in this smoothed shape. The location and height of the wrinkles are clearly highlighted in the wrinkle plot, Fig. 3(d). In these contour plots, and all subsequent ones, the horizontal direction corresponds to the 0° direction of the weft tows and the direction of stitching. Regions of positive wrinkle height in red correspond to parts of the fabric further away from the mould, and regions of negative wrinkle height in blue are closer to the mould. The inner blue circle included in Fig. 3(d) plots the extent of the nominal contact patch between the mould and the fabric, for the case illustrated with a punch displacement of 75 mm. Figure 3(e) plots a 3D surface reconstruction of this data. The full data set of 3D height data is available in the online data repository.

Finally, to characterise the wrinkles, the wrinkle height is extracted on a circle at a radius of 110 mm from the centre of the blank, marked by the magenta circle on Fig. 3(d). This radius was chosen as typical of the location where the maximum wrinkle deformation occurred.

Figure 4 plots this wrinkle amplitude for the case shown in Fig. 3. The orientation angle θ is as indicated on Fig. 3(d). The severity of wrinkling is quantified by the root-mean-square (r.m.s.)

amplitude of the wrinkle profile and the maximum peak-to-trough height of the wrinkle. The number of wrinkles is characterised by the number of distinct peaks and troughs around the circumference of height or depth greater than the r.m.s. wrinkle amplitude and more than 20° apart (so as to avoid double-counting small peaks on the same wrinkle). The critical peaks and troughs greater than the r.m.s. amplitude are identified by circles in Fig. 4. For the data given in Figs. 3 and 4 these values for the r.m.s. amplitude and number of peaks are 1.67 mm and 11, respectively.

3 Results

3.1 Repeatability study

Repeatability studies were undertaken for two cases. Figure 5(a) shows results for the light triaxial fabric with a clamping weight of 4 kg, plotting the evolution of the wrinkle r.m.s. height with punch displacement for the five repeats undertaken. The standard deviation of wrinkle amplitudes for the five repeats at a final punch displacement of 75 mm is 0.32 mm, equal to 9 % of the mean value of 3.5 mm. Similarly good agreement is seen for results with six repeats for the $\pm 45^\circ$ biaxial fabric with a clamping weight of 2 kg, where the standard deviation of wrinkle amplitude at a final punch displacement of 75 mm is 0.12 mm, equal to 5 % of the mean amplitude of 2.3 mm. These results are plotted in Fig. 5(b). The corresponding wrinkle patterns for the light triaxial fabric are shown in Figs 6(a) to (e). The repeatability of wrinkle patterns is good, with a broadly similar pattern for all the tests, albeit with the exact locations of positive and negative wrinkles varying from sample to sample. This is further illustrated in Fig. 6(f), which plots the wrinkle height as a function of orientation around a circle at a radius of 100 mm from the centre of the blank.

3.2 Wrinkle amplitude

Figures 7 (a) to (f) plot the evolution of the wrinkle r.m.s. height with punch displacement for the different fabrics. Similar results are seen for the maximum peak-to-trough wrinkle amplitudes. The wrinkle amplitude increases roughly linearly with punch displacement for the $\pm 45^\circ$ and $\pm 60^\circ$ biaxial fabrics and the two triaxial fabrics, Figs. 7 (b, c, e-f). For the unidirectional and 0/90° biaxial fabrics the amplitude of wrinkling is much smaller, corresponding to small deviations in shape rather than significant wrinkling. This reflects the effective biaxial nature of these fabrics (taking into account the stitching constraint), which allows relatively easy shear deformation of

the fabrics following the pin-jointed net mechanism. The exception to this are the results for the 0/90° biaxial fabric with no additional weights (Fig. 7d), where the wrinkle amplitude does increase significantly with punch displacement, albeit at a smaller level than for the other fabrics. Apparently the in-plane forces associated with clamping are able to promote shear over wrinkling for this easily-sheared material [11]. While the significant wrinkle deformation for the other fabrics, and especially for the two triaxial fabrics, reflects the way in which shear of these fabrics cannot occur without significant tow slippage or stitch deformation [13].

The progressive increase in amplitude with deformation is consistent with the low bending resistance of dry fabrics [8]. The resistance to in-plane deformation of the fabric limits the way that progressive changes in the shape of the fabric can be accommodated by shear deformation. The remaining geometric mismatch between the fabric and wrinkle-free deformed shape needs to be accommodated by wrinkling in a way which increases with the deformation. This has been shown to depend both on shear and compressive stresses generated within the fabric [8, 11]. Increases in clamping force alter this picture by modifying the fabric slip at the boundary of the blank and the geometric changes developed in the fabric due to membrane stresses [11].

Note that poor image quality in the unidirectional fabric, due to the lack of contrast between the tows and the black carbon stitching, meant that poor quality height maps were produced at some punch displacements with weights of 0 and 8 kg. These results have been omitted. Modifications to lighting or addition of a paint spray pattern would be needed to improve these measurements. Other data points or curves missing from the sets of curves (e.g. unidirectional material with a 2 kg weight and $\pm 60^\circ$ biaxial fabric with a 0 kg weight) correspond to situations where tests were not undertaken, in general due to a shortage of material.

The effect of clamping weight on wrinkle amplitude for all the fabrics is summarised in Fig. 8, plotting results for the maximum punch deformation of 75 mm. One estimate of the error associated with these results is given by the two repeatability case studies, where the error bars (marked by asterisks) shown on Fig. 8 give \pm one standard deviation. Further quantification of the reliability of the measurements is provided by calculating the wrinkle height for each half of the blank, taking advantage of symmetry to derive two independent measures of wrinkling. These two wrinkle amplitudes are included on Fig. 8 for each of the conditions where the repeatability tests were not carried out. The range indicated by these measurements is similar

to the standard deviation in the repeatability tests, confirming this estimate of the accuracy of the measurements. Hence relatively small changes, for example the dip at a weight of 1 kg for the heavy triaxial load, or variations across the weight range for the $\pm 45^\circ$ biaxial fabric, should be disregarded. Nevertheless broad trends can be observed in these results. There is a general trend for increasing clamping ring weight to reduce the wrinkling, particularly for the high-amplitude wrinkles seen in the triaxial fabrics. However, over the range of clamping weights tested, there is still significant wrinkling for these materials. Moreover addition of clamping weights has relatively little effect on the wrinkle amplitude of the $\pm 45^\circ$ and $\pm 60^\circ$ biaxial fabrics, despite these being the two lowest weight fabrics. While even a small amount of weight is able to eliminate wrinkling for the $0/90^\circ$ fabric. The larger effect of clamping for the light triaxial fabric, compared with the heavy triaxial fabric, may reflect the difference in weights of these materials, although the differences both in wrinkle amplitude and weight are relatively small. Note that the $0/90^\circ$ fabric has the lowest amplitude of wrinkling, despite this being the heaviest weight material, again because of its good shear properties. In summary, addition of clamping weights can be helpful but it does not appear to be a panacea which can eliminate wrinkling in fabrics which are susceptible to this defect. Moreover the usefulness of clamping depends on the material, in a way that does not depend as much on fabric weight as on the details of the fabric architecture. Perhaps a further increase in clamping weight could have the desired effect, but the corresponding increase in in-plane tension might lead to damage to the fabric architecture.

3.3 Wrinkle patterns

The pattern of wrinkling provides valuable information both for validation studies and to give clues as to the relevant mechanisms of wrinkling and strategies to avoid this. Figure 9 shows contour plots, for the six fabrics, of the wrinkling height pattern at a punch displacement of 50 mm with a clamping weight of 4 kg. Recall that in all these contour plots the 0° warp and stitching directions runs horizontally, so that this is a line of symmetry of the fabric. The colour scales for the wrinkle height are the same in all the plots, allowing comparison of both the amplitude and pattern of wrinkles. As noted above, there insignificant wrinkling in the unidirectional material, Fig. 9(a). Similarly the $0/90^\circ$ biaxial fabric, Fig. 9 (d), has relatively little wrinkling for the case shown, with small amounts of wrinkling at the 0° , 180° and $\pm 90^\circ$ locations. These are the locations where the tows run in the radial and circumferential directions, so that the fabric cannot accommodate the required reduction in peripheral length as the drape progresses by shearing deformation. Such

shearing deformation would result in elongation in the radial direction, resisted by the stitching or tows. For the $\pm 45^\circ$ biaxial fabric, Fig. 9 (b), wrinkling is predominantly observed at the 0° and 180° positions, but with some indication of wrinkling extending further away from the horizontal axis. Although the tows are rotated by 45° relative to the $\pm 90^\circ$ fabric, the additional constraint of the stitching in the 0° direction means that this fabric does not deform in the same way as the $\pm 90^\circ$ fabric, but rotated through 45° . Specifically the stitching prevents shearing of the material at the 0° and 180° positions, which would be needed to reduce the length of the circumference as the blank is drawn in. For the $\pm 60^\circ$ biaxial fabric, Fig. 9 (c), there is a more complex pattern of wrinkling, with wrinkling seen around most of the periphery. Finally the two triaxial fabrics, Figs. 9 (e) and (f), have wrinkling distributed around much of the circumference, although there seems to be a particularly strong band of wrinkling at the 0° and 180° positions, associated with the difficulty of shearing in these locations due to both the tows and the stitching.

To confirm the observation of progressive wrinkling inferred above, Fig. 10 shows the change in wrinkle pattern with increasing punch deformation for the light triaxial fabric under a clamping weight of 8 kg. The height colour scale bars have been adjusted to emphasise the pattern in each case. It is clear that the wrinkle pattern developed early in the drape persists with increasing deformation. However the wrinkles at the 0° and 180° positions grow more to provide the most predominant features at the final deformation step, Fig 10 (d).

The effect of clamping weight in altering the wrinkle pattern is illustrated in Fig. 11, again for the light triaxial fabric at the maximum punch displacement of 75 mm. Here the scalebars are the same for each plot. With no additional clamping weight, Fig 11 (a), wrinkles are predominantly seen at the 0° and 180° directions. Addition of 4 kg clamping weights reduces significantly the magnitude of wrinkles at these locations, but additional wrinkling at 0° and 90° occurs. At the heaviest weight of 8 kg, these wrinkles at the 0° and 90° directions are suppressed, while the wrinkles at 0° and 180° remain. This more complicated picture reflects the complications in wrinkling observed previously [8, 13], in which contributes from shear and compressive stresses affect the results. The clamping forces will modify both the shear deformation and the in-plane membrane stresses, in a way that makes it difficult to predict how the wrinkle pattern will depend on clamping forces. In this case, perhaps localisation of wrinkling at the 0° and 180° directions occurs at the lowest clamping load as a high degree of pull-in of the material there through the clamping ring causes a reduction of the constraint at that point. At the intermediate

load friction may prevent such large pull-in and localisation, giving rise to wrinkling distributed around the structure, and specifically at the $\pm 90^\circ$ locations. While at the highest load of 8 kg, the in-plane stresses generated through the structure may now inhibit wrinkling at the $\pm 90^\circ$ locations, leaving only the wrinkling at the 0° and 180° locations which are more constrained from shearing by both tows and stitching. This discussion emphasises the need for effective modelling of such behaviour, with models validated by experiments such as those presented in this paper. In addition the assessment and modelling of friction distributions around the clamping rings will be needed to predict this behaviour.

Figure 12 provides further evidence of the differences in wrinkling pattern as a function of fabric and clamping weight, plotting the number of wrinkles (i.e. number of peaks and troughs) at a maximum punch displacement of 75 mm. In the absence of clamping weight, all the fabrics have about 10 wrinkles around the circumference. This corresponds to a relatively simple wrinkling pattern, either with wrinkles at $\pm 90^\circ$ positions for the $0/90^\circ$ fabric (see Fig 9 d) or, for the other biaxial and triaxial fabrics, with wrinkles at the 0° and 180° locations. At the higher clamping loads the increase in the number of wrinkles in the two triaxial fabrics corresponds to the development of a more complex wrinkling pattern, see Figs. 9 (e) and (f). Again the changes in wrinkle distribution with material and clamping load reflect a complex interplay between the membrane stresses generated in the fabric and the shear resistance due to the material architecture [11]. The full set of wrinkle height data is available at the online data repository.

4 Conclusions

The aim of this paper is to provide a simple method to characterise wrinkle formation when forming non-crimp carbon fabrics over a male hemispherical mould. The following conclusions can be drawn.

- The forming rig, imaging system and shape-from-focus image analysis technique described in this paper provide a simple and effective means for characterising wrinkle formation during draping of non-crimp fabrics. Other measurement parameters, for example fibre angle using image correlation (e.g. [28, 29]) or fabric blank pull-in from observations through the transparent blank-holder (e.g. [17]), could be straightforwardly incorporated.

- Repeatability of both the wrinkle amplitude and wrinkle pattern is good, with the standard deviations in wrinkle amplitude equal to 5 and 9 % of the mean amplitude, for the two cases considered.
- The wrinkle amplitude increases progressively with punch deformation.
- The wrinkle amplitude depends critically on the fabric architecture. Unidirectional and 0/90° biaxial fabrics had the smallest wrinkle amplitudes, $\pm 45^\circ$ and $\pm 60^\circ$ biaxial fabrics had intermediate amplitudes and the two triaxial fabrics tested had the largest wrinkle amplitudes.
- The pattern of wrinkling depends both on the fabric and the clamping load. However, the effect of clamping load is not straightforward, being less effective for some materials than others. The highest clamping weights tested were not effective at eliminating wrinkles in four of the fabrics tested.
- Measurements of wrinkle deformation patterns and forming loads provide a useful data set for validating models of wrinkling in non-crimp fabrics. The hope is that such models can provide an effective way to optimise material architecture and drape procedures for complex shapes.

Acknowledgements

The authors are grateful for advice and materials from John Klintworth (Dassault Systèmes), Paul Bristo (Jaguar Land Rover Ltd.), Liam O'Sullivan and Tom James (Formax). The contributions from an exploratory MEng project by Jack Tawney and the practical assistance of Alan Heaver are also gratefully acknowledged. The helpful comments of anonymous reviewers are also gratefully acknowledged.

Appendix

This appendix gives details of a calibration check on the height analysis methodology, imaging and analysing a piece of white card, formed into a cone of the same height (77 mm) and diameter as the deformed blank, and sprayed with black paint to create a speckle pattern. The shape-from-focus method itself has been well documented, and the raw height images of Fig. 3(a) confirm that the fabric images used have an appropriate set of features to apply this methodology and derive a smooth surface map. Hence the calibration setup was chosen especially to validate the height extraction from the images. Figure A1 shows a typical photograph of the card. The black rectangles are pieces of adhesive tape holding the cone in

place. Figure A2 shows the raw height data of individual pixels, in terms of stack height (i.e. picture numbers, non-integer values result from interpolation). Note that these analysis images are flipped relative to the photo. Black regions do not give useful height data. Figure A3 gives the corresponding height data, after applying a median filter and scaling in the height and in-plane directions. Figure A4 compares the estimated height along a radius with the cone profile. Agreement is good.

References

1. Kong H, Mouritz AP, Paton R. Tensile extension properties and deformation mechanisms of multiaxial non-crimp fabrics *Composite Structures* 2004;66:249–259.
2. Truong TC, Vettor Mi, S Lomov, Verpoest I. Carbon composites based on multi-axial multi-ply stitched preforms. Part 4. Mechanical properties of composites and damage observation. *Composites Part A* 2005;36:1207-1221.
3. Middendorf P, Metzner C. Aerospace applications of non-crimp fabric composites. In *Non-crimp fabric composites. Manufacturing, properties and applications*, Ed. SV Lomov, Woodhead Publishing 2011, pp441-448.
4. Sköck-Hartmann B, Gries T. Automotive applications of non-crimp fabric composites. In *Non-crimp fabric composites. Manufacturing, properties and applications*. Ed. SV Lomov, Woodhead Publishing 2011, pp461-480.
5. Harrison P, Yu W-R, Long AC. Modelling the deformability of biaxial non-crimp fabric composites. In *Non-crimp fabric composites. Manufacturing, properties and applications*, Ed. SV Lomov, Woodhead Publishing 2011 pp144-165.
6. Lee JS, Hong SJ, Yu WR, Kang TJ. The effect of blank holder force on the stamp forming behavior of non-crimp fabric with a chain stitch. *Compos Sci Technol* 2007; 67:357–366.
7. Gereke T, Döbrich O, Hübner M, Cherif C. Experimental and computational composite textile reinforcement forming: A review. *Composites: Part A* 2013;46:1-10.
8. Boisse P, Hamila N, Vidal-Sallé E, Dumont F. Simulation of wrinkling during textile composite reinforcement forming. Influence of tensile, in-plane shear and bending stiffnesses. *Compos Sci Technol* 2011;71:683–692.

9. Allaoui S, Boisse P, Chatel S, Hamila N, Hivet G, Soulat D, Vidal-Salle E. Experimental and numerical analyses of textile reinforcement forming of a tetrahedral shape. *Composites: Part A* 2011;42:612–622.
10. Pazmino J, Carvelli V, Lomov SV. Formability of a non-crimp 3D orthogonal weave E-glass composite reinforcement. *Composites: Part A* 2014;61:76–83.
11. Lin H, Wang J, Long AC, Clifford MJ, Harrison P. Predictive modelling for optimization of textile composite forming. *Compos Sci Technol* 2007;67:3242–52.
12. Bel S, Boisse P, Dumont F. Analyses of the deformation mechanisms of non-crimp fabric composite reinforcements during preforming. *Appl Compos Mater* 2012;19:513–528.
13. Yu WR, Harrison P, Long A. Finite element forming simulation for non-crimp fabrics using a non-orthogonal constitutive equation. *Composites: Part A* 2005;36:1079–1093.
14. Creech G, Pickett AK. Meso-modelling of non-crimp fabric composites for coupled drape and failure analysis. *J Mat Sci* 41 6725-6736 2006
15. Al-Gaadi B, Göktepe F, Halász M. A new method in fabric drape measurement and analysis of the drape formation process *Textile Research Journal* 2012;82(5):502–512.
16. Domskienė J, Strazdienė E, Bekampienė P. Development and optimisation of image analysis technique for fabric buckling evaluation. *International Journal of Clothing Science and Technology* 2011;23(5):329-340.
17. Christ M, Miene A, Moerschel U. Characterization of the drapability of reinforcement fabrics by means of an automated tester, In: *Proc. 12th Annual Automotive Composites Conference and Exhibition*. Troy, USA, 2012. p.633-645.
18. Ouagne P, Soulat D, Moothoo J, Capelle E, Gueret S. Complex shape forming of a flax woven fabric; analysis of the tow buckling and misalignment defect. *Composites: Part A* 2013;51:1–10.
19. Lomov SV, Boisse P, Deluycker E, Morestin F, Vanclooster K, Vandepitte D, Verpoest I, Willems A. Full-field strain measurements in textile deformability studies. *Composites: Part A* 2008;39:1232–1244.
20. Arnold S, Sutcliffe MPF, Oram WLA. Experimental measurement of wrinkle formation during draping of non-crimp fabric. <https://www.repository.cam.ac.uk/handle/1810/252589>, 2015.
21. Nayar SK, Nakagawa Y. Shape from focus. *IEEE Transactions on Pattern analysis and Machine Intelligence* 1994;16:824-831.

22. Pertuz S, Puig D, Garcia MA. Reliability measure for shape-from-focus. *Image and Vision Computing* 2013;31(10):725-734.
23. Pertuz S, Puig D, Garcia MA. Analysis of focus measure operators for shape-from-focus. *Pattern Recognition* 2013;46(5):1415-1432.
24. Pertuz S. Focus Measure, A function to measure the relative degree of focus of an image. 2010. <http://www.mathworks.com/matlabcentral/fileexchange/27314-focus-measure/content/fmeasure/fmeasure.m>, accessed 30th August 2015.
25. D'Errico J. Surface fitting using gridfit. 2005. <http://uk.mathworks.com/matlabcentral/fileexchange/8998-surface-fitting-using-gridfit>, accessed 7th November 2015.
26. Davies ER. *Machine Vision: Theory, Algorithms, Practicalities*. Chapter 10. 3rd Edition. Morgan Kaufman Publishers, 2005.
27. Gonzalez RC, Woods RE, Eddins SL, *Digital image processing using Matlab*. 2nd Edition, Gatesmark Publishing, 2009.
28. Skordos AA, Sutcliffe MPF. Stochastic simulation of woven composites forming, *Composites Science and Technology* 2008;68:283-296.
29. Pazmino J, Carvelli V, Lomov SV, Van Mieghem B, Lava P. 3D digital image correlation measurements during shaping of a non-crimp 3D orthogonal woven E-glass reinforcement. *Int J Mater Form* 2014;7:439–446.

Figure captions

Figure 1. Schematic of rig

Figure 2. Photograph of deformed heavy triaxial fabric blank and surrounding supporting ring (of inner diameter 287 mm).

Figure 3. Example of wrinkle characterisation methodology, showing the region of the fabric blank visible through the supporting ring of internal diameter 287 mm. The fabric 0° weft tows and stitching direction runs horizontally in these and subsequent contour plots. (a) raw height data, (b) total shape height data, (c) smoothed shape, (d) wrinkle height, (e) three-dimensional representation of fabric shape. (Results for light triaxial fabric, 8 kg weights, 75 mm punch displacement.)

Figure 4. Wrinkle height around a circle at a radius of 110 mm, (as illustrated by the magenta circle in Fig. 3(d)). Same test case as Fig. 3. The angle θ is as indicated on Fig. 3 (d). Red circles identify peaks and troughs.

Figure 5. Repeatability of evolution of wrinkle height with punch displacement: (a) light triaxial fabric with 4 kg weights, (b) $\pm 45^\circ$ biaxial fabric with 2 kg weights.

Figure 6. Repeatability of drape wrinkle pattern for light triaxial fabric with 4 kg weights at a maximum punch displacement of 75 mm: (a) – (e) wrinkle height contours for the repeat tests, (f) wrinkle heights around a circle at a radius of 110 mm.

Figure 7. Effect of punch displacement and clamping weight on wrinkle height for different fabrics: (a) unidirectional, (b) $\pm 45^\circ$ biaxial, (c) $\pm 60^\circ$ biaxial, (d) $0/90^\circ$ biaxial, (e) light triaxial, (f) heavy triaxial.

Figure 8. Effect of clamping weight on the wrinkle height at a maximum punch displacement of 75 mm. The error bars indicated by asterisks give \pm one standard deviation of the results for the two repeatability cases. The range indicated for the other conditions plots the values for the two halves of each blank.

Figure 9. Wrinkle height contours for the different fabrics at a maximum punch displacement of 50 mm with 4kg weights: (a) unidirectional, (b) $\pm 45^\circ$ biaxial, (c) $\pm 60^\circ$ biaxial, (d) $0/90^\circ$ biaxial, (e) light triaxial, (f) heavy triaxial.

Figure 10. Wrinkle height contours for the light triaxial fabric, 8 kg weight, at punch displacements of: (a) 20 mm, (b) 40 mm, (c) 60 mm, (d) 75 mm.

Figure 11. Wrinkle height contours for the light triaxial fabric, at a punch displacement of 75 mm at different clamping weights of: (a) 0 kg, (b) 4 kg (c) 8 kg.

Figure 12. Effect of clamping weight on the number of wrinkle peaks and troughs around the circumference at a maximum punch displacement of 75 mm.

Figure A1. Typical image from the calibration cone. Black rectangles are adhesive tapes.

Figure A2. Raw height data for the calibration case, taken from the shape-from-focus analysis. The magenta circle marks the extent of the cone, located using the Hough transform algorithm.

Figure A3. Scaled height data from the calibration case.

Figure A4. Variation in height data along a radius for the cone calibration case. The actual cone geometry is marked by the straight line.

Table 1. Materials tested. Note that the $\pm 60^\circ$ biaxial fabric is powder-bound.

Material	Formax designation	Tow directions	Weight (g/m ²)	Filaments per tow	Stitching
Unidirectional	FCIM321	0°	600	24k	Weft fibres
$\pm 45^\circ$ biaxial	FCIM105	$\pm 45^\circ$	400	12k	2.22 mm pillar
$\pm 60^\circ$ biaxial	FCIM342-L.	$\pm 60^\circ$	440	24k	2.12 mm tricot
0/90° biaxial	FCIM603	0/90°	800	24k	3.33 mm tricot
Light triaxial	n/a	-45/+45/0°	600	24k	2.0 mm tricot
Heavy triaxial	FCIM358	-45/+45/0°	750	24k	2.12 mm pillar

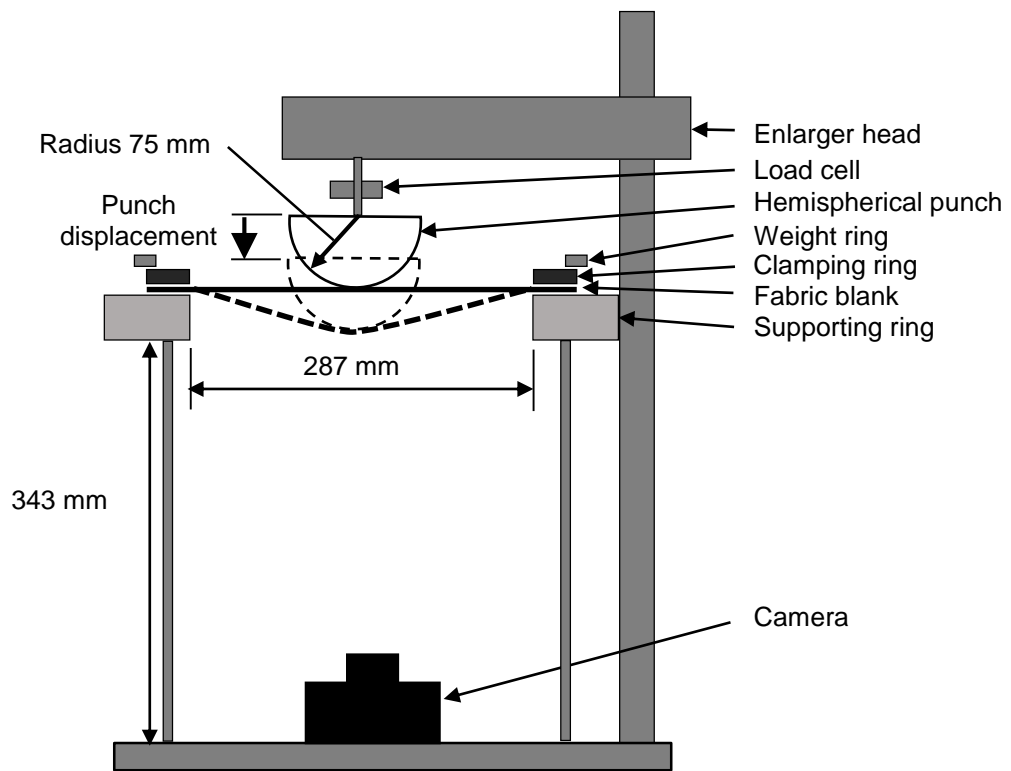


Figure 1. Schematic of rig

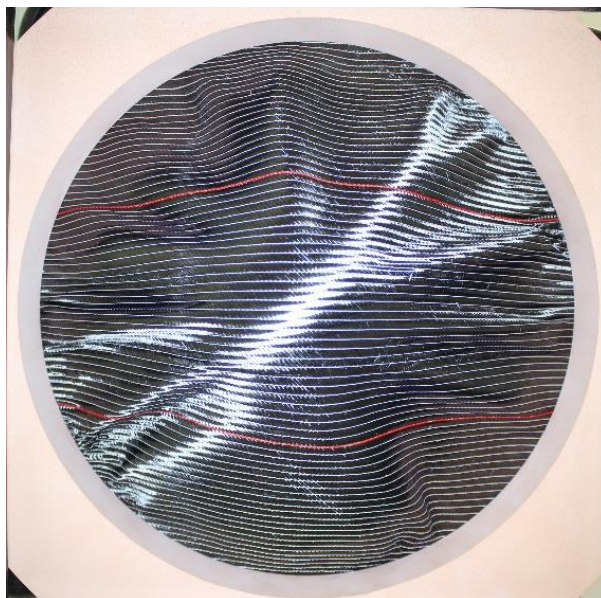


Figure 2. Photograph of deformed heavy triaxial fabric blank and surrounding supporting ring (of inner diameter 287 mm).

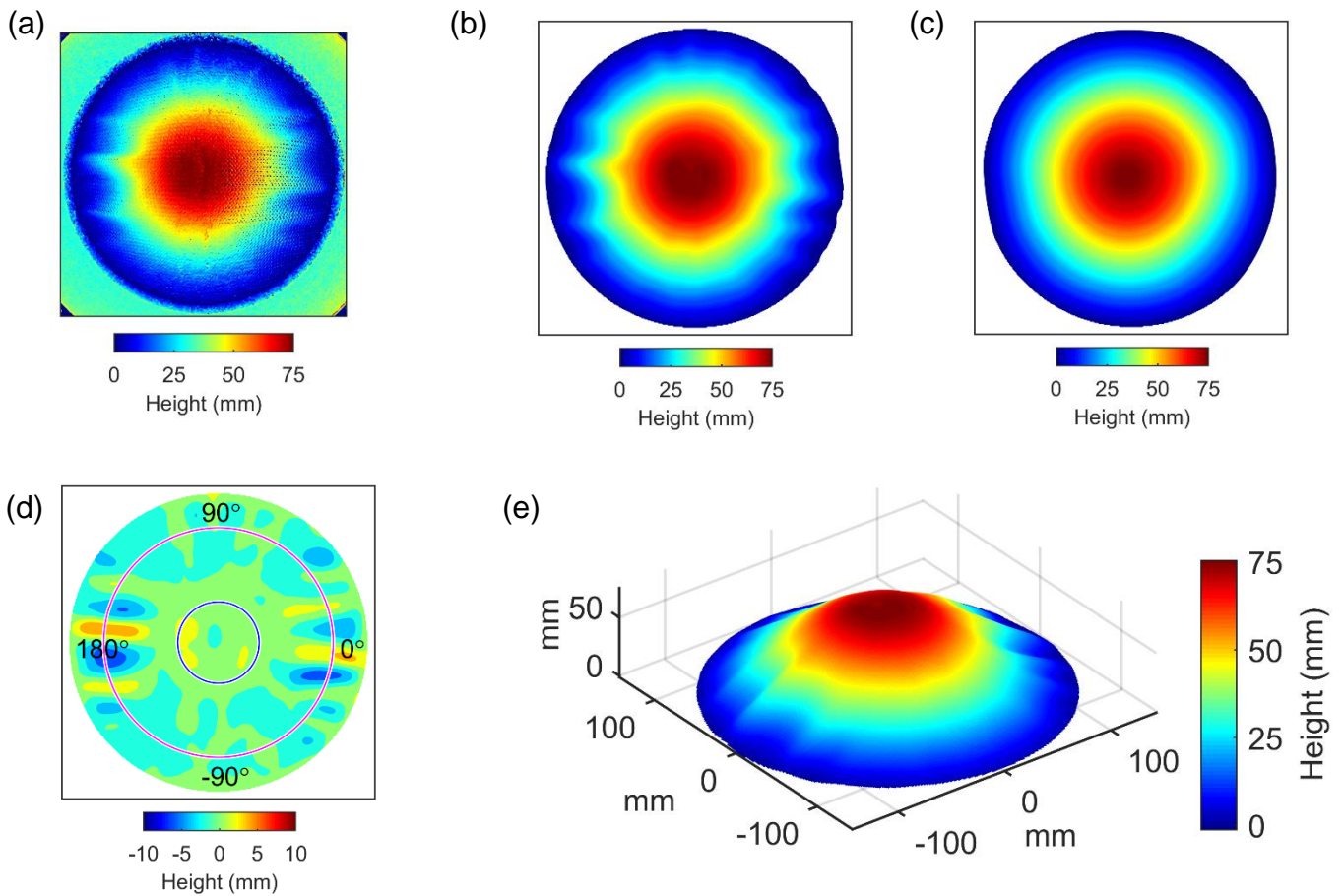


Figure 3. Example of wrinkle characterisation methodology, showing the region of the fabric blank visible through the supporting ring of internal diameter 287 mm. The fabric 0° weft tows and stitching direction runs horizontally in these and subsequent contour plots. (a) raw height data, (b) total shape height data, (c) smoothed shape, (d) wrinkle height, (e) three-dimensional representation of fabric shape. (Results for light triaxial fabric, 8 kg weights, 75 mm punch displacement.)

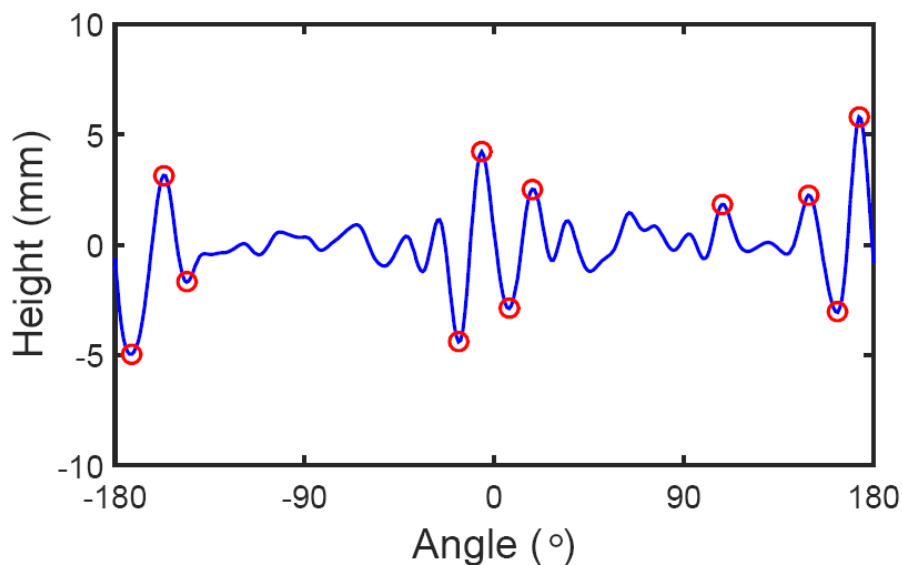


Figure 4. Wrinkle height around a circle at a radius of 110 mm, (as illustrated by the magenta circle in Fig. 3(d)). Same test case as Fig. 3. The angle θ is as indicated on Fig. 3 (d). Red circles identify peaks and troughs.

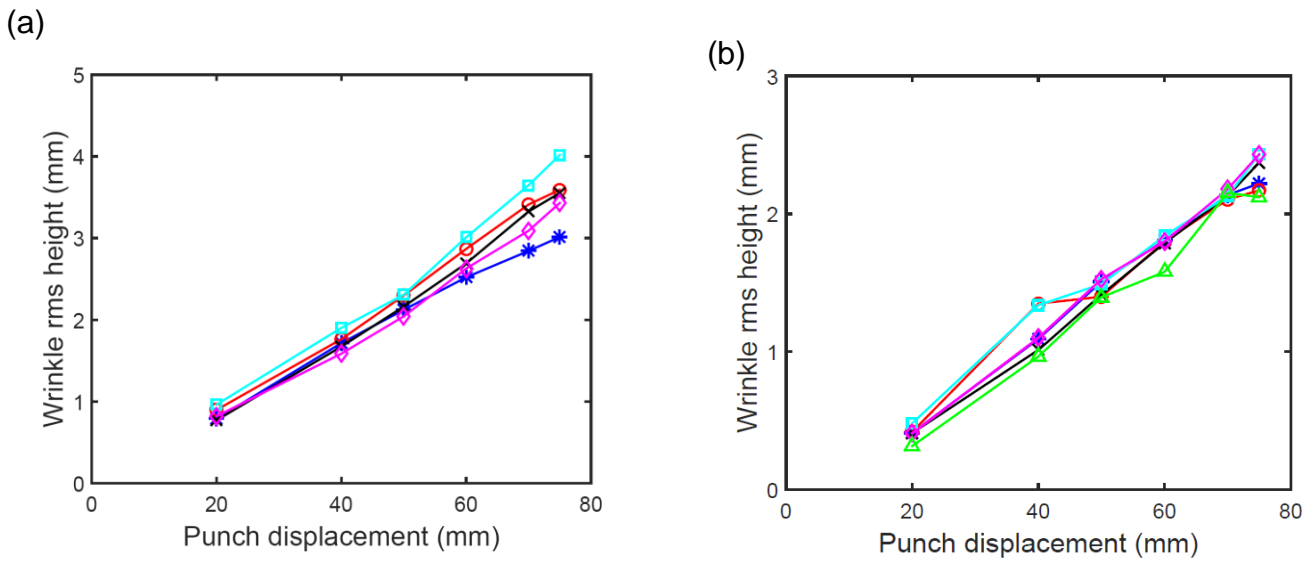


Figure 5. Repeatability of evolution of wrinkle height with punch displacement: (a) light triaxial fabric with 4 kg weights, (b) $\pm 45^\circ$ biaxial fabric with 2 kg weights.

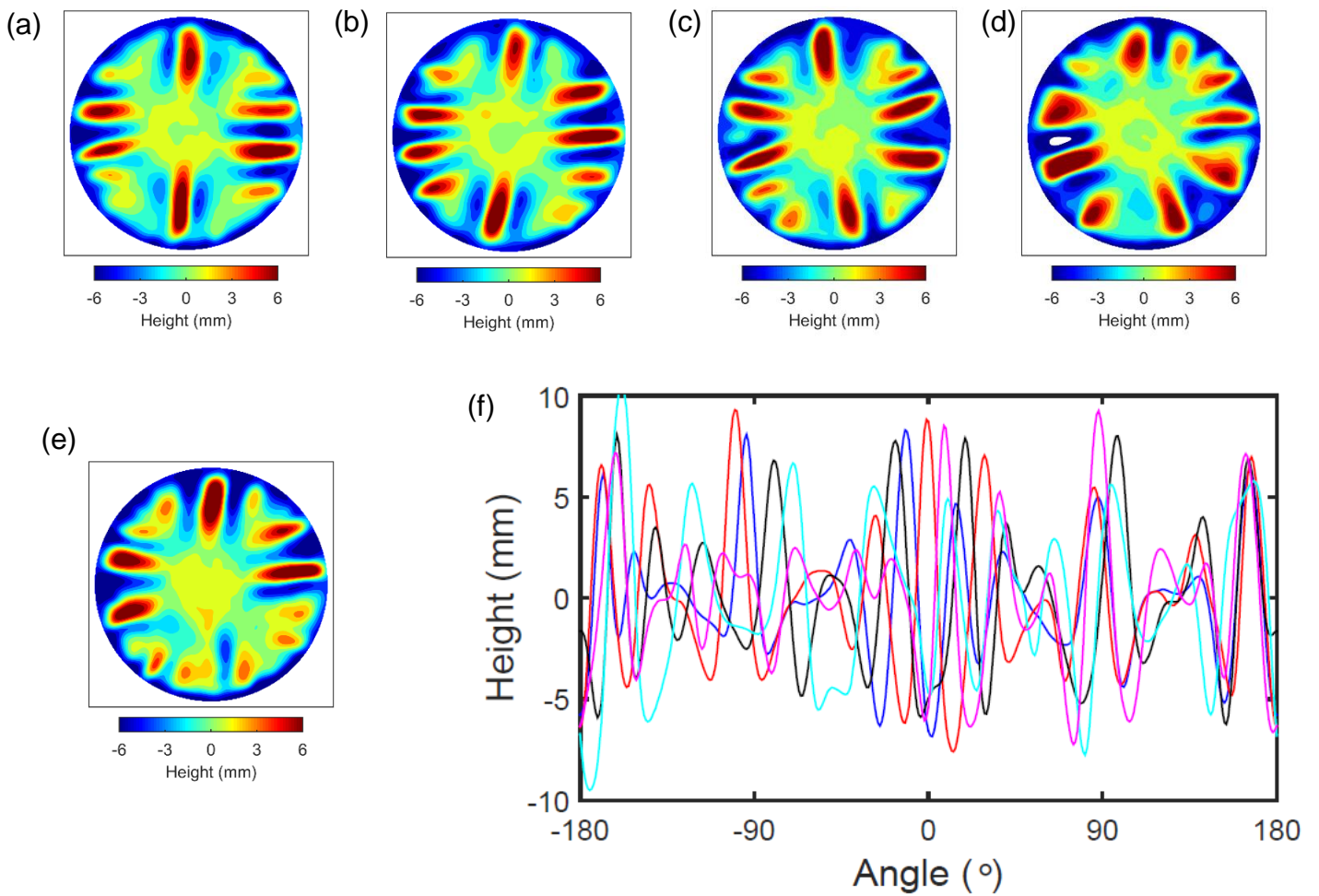


Figure 6. Repeatability of drape wrinkle pattern for light triaxial fabric with 4 kg weights at a maximum punch displacement of 75 mm: (a) – (e) wrinkle height contours for the repeat tests, (f) wrinkle heights around a circle at a radius of 110 mm.

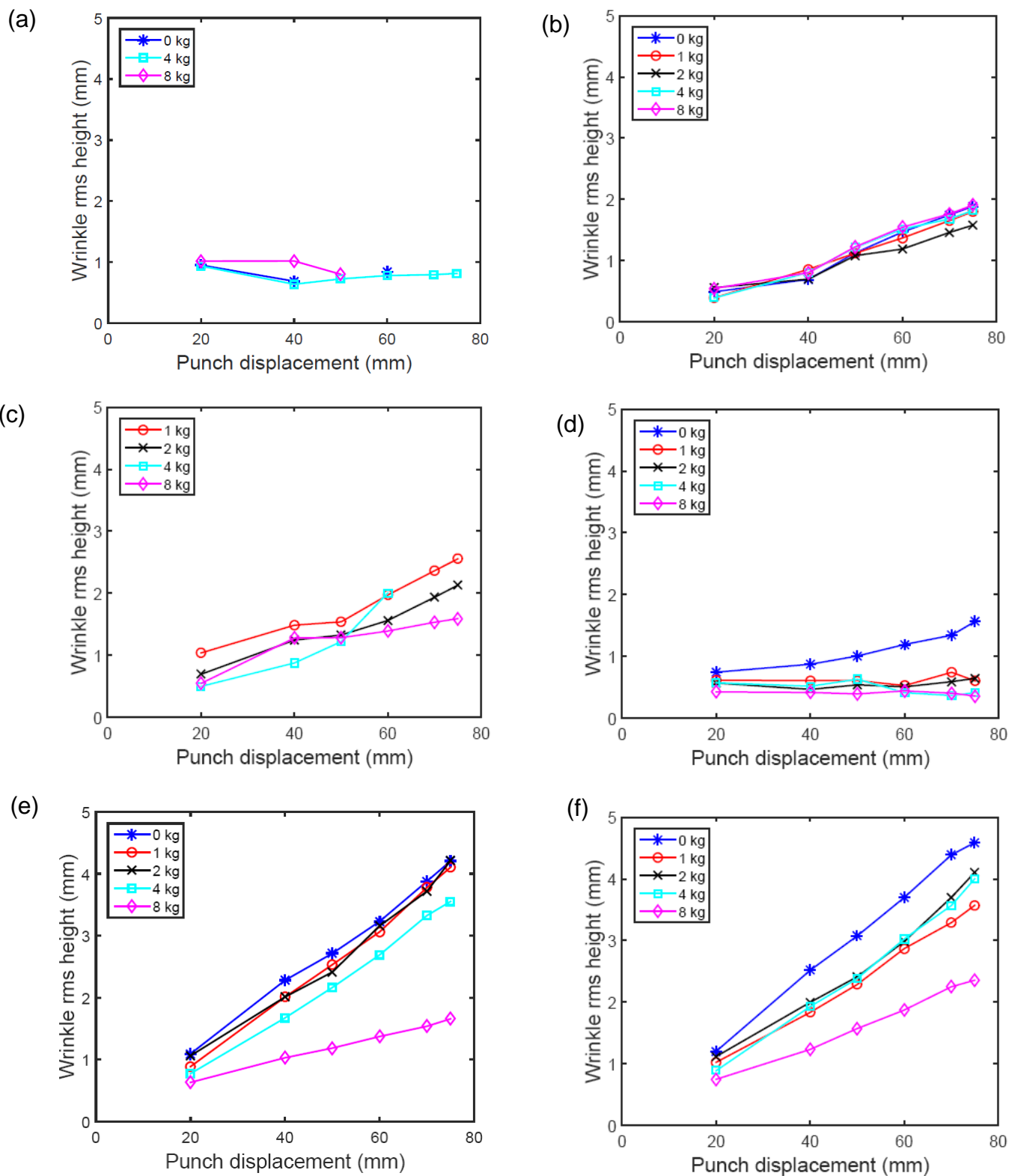


Figure 7. Effect of punch displacement and clamping weight on wrinkle height for different fabrics: (a) unidirectional, (b) $\pm 45^\circ$ biaxial, (c) $\pm 60^\circ$ biaxial, (d) $0/90^\circ$ biaxial, (e) light triaxial, (f) heavy triaxial.

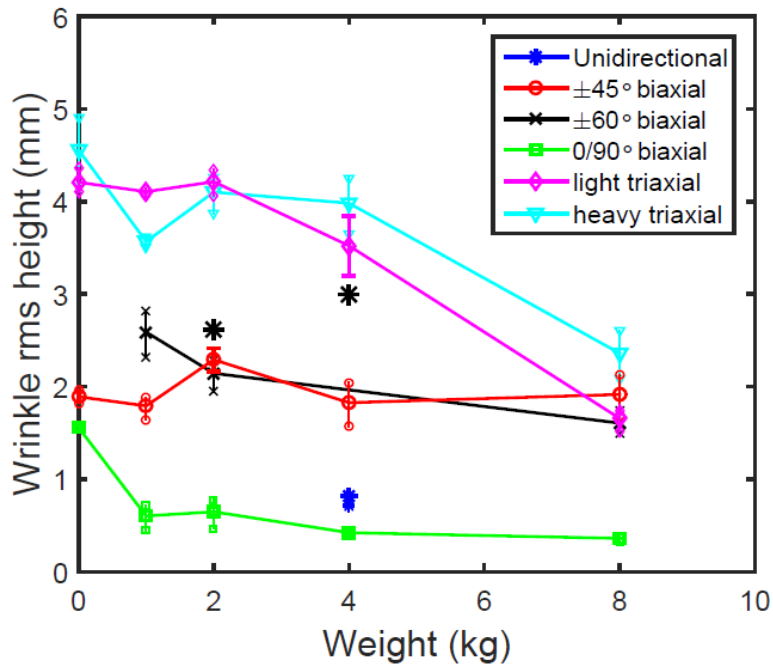


Figure 8. Effect of clamping weight on the wrinkle height at a maximum punch displacement of 75 mm. The error bars indicated by asterisks give \pm one standard deviation of the results for the two repeatability cases. The range indicated for the other conditions plots the values for the two halves of each blank.

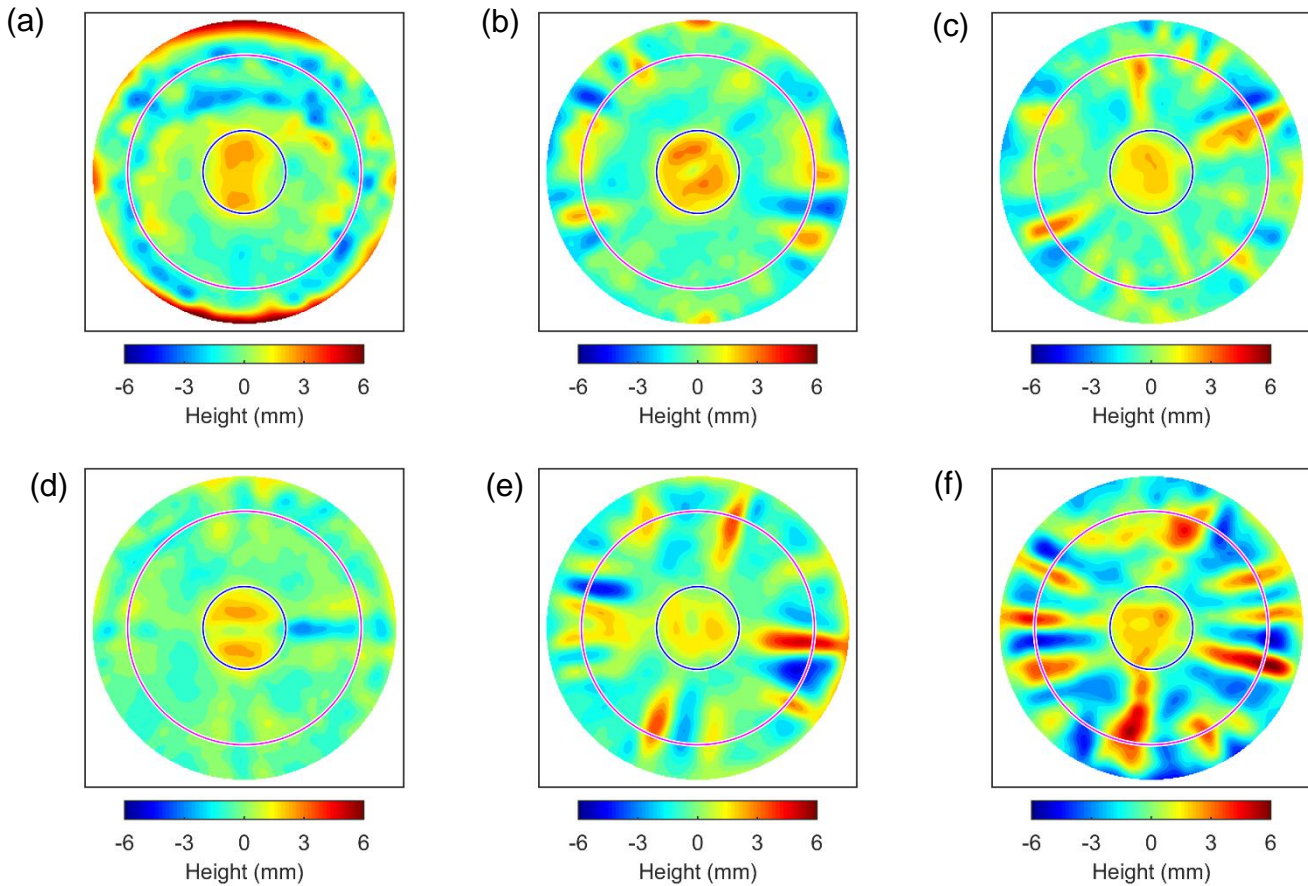


Figure 9. Wrinkle height contours for the different fabrics at a punch displacement of 50 mm with 4 kg weights: (a) unidirectional, (b) $\pm 45^\circ$ biaxial, (c) $\pm 60^\circ$ biaxial, (d) 0/90° biaxial, (e) light triaxial, (f) heavy triaxial.

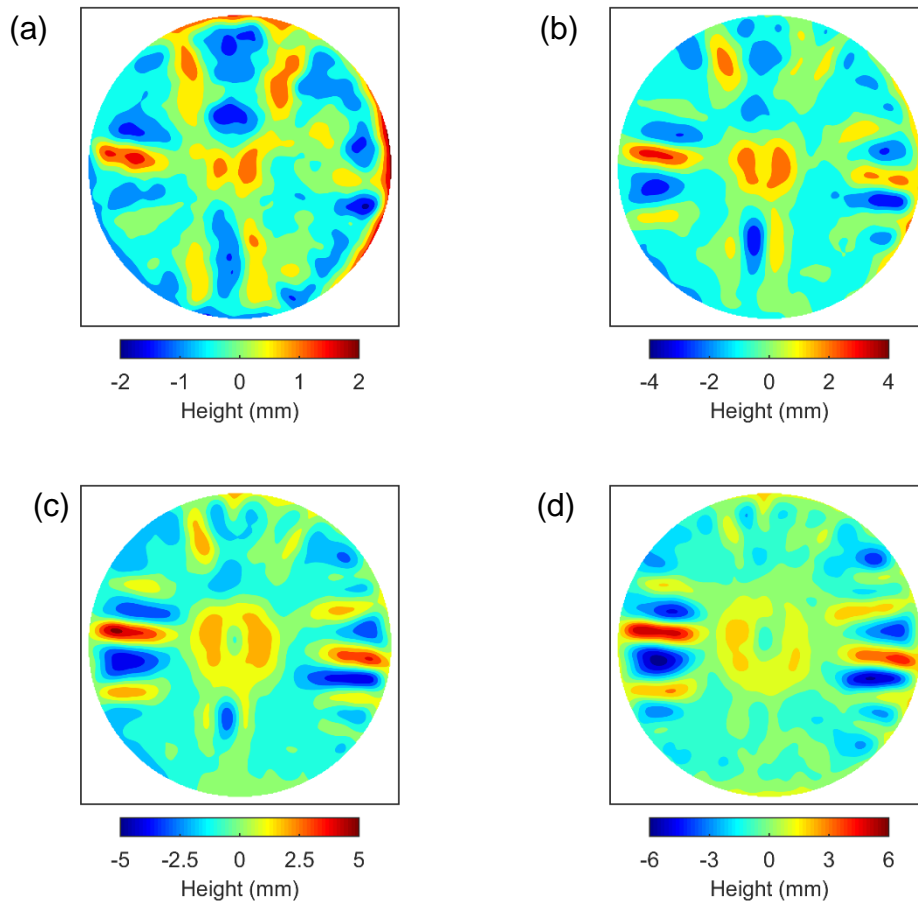


Figure 10. Wrinkle height contours for the light triaxial fabric, 8 kg weights, at punch displacements of: (a) 20 mm, (b) 40 mm, (c) 60 mm, (d) 75 mm.

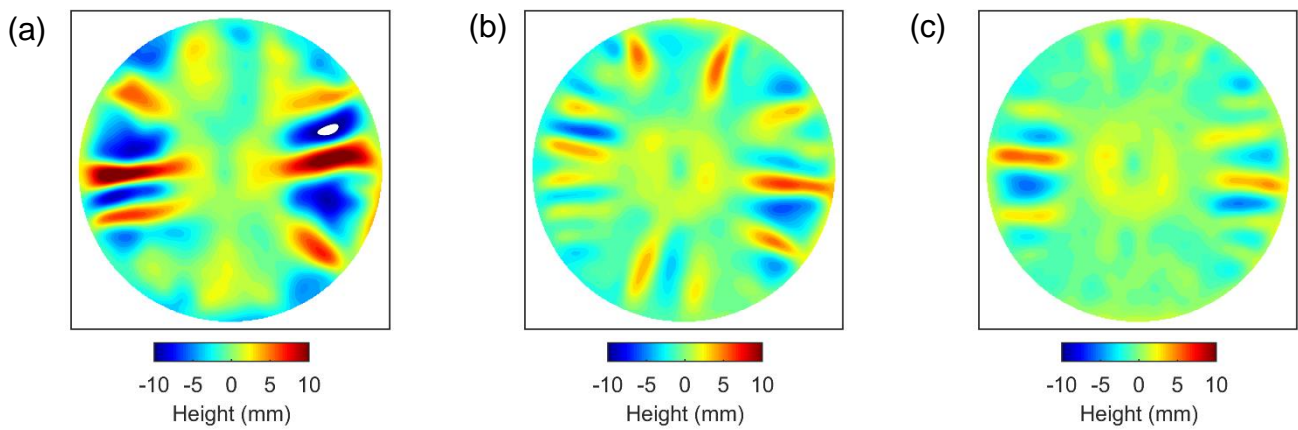


Figure 11. Wrinkle height contours for the light triaxial fabric, at a punch displacement of 75 mm, with different clamping weights of: (a) 0 kg, (b) 4 kg, (c) 8 kg.

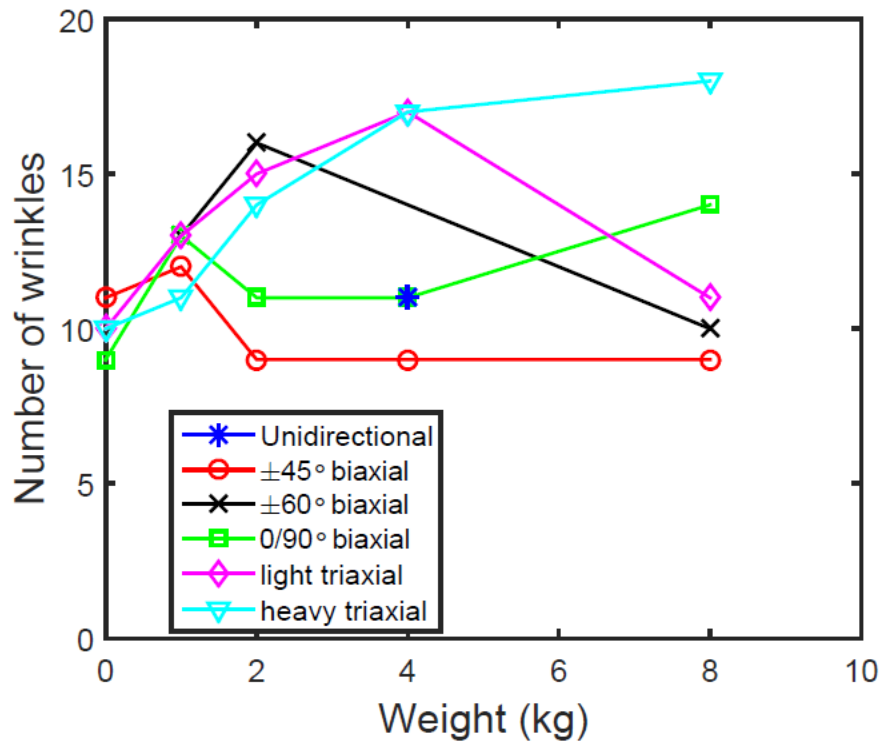


Figure 12. Effect of clamping weight on the number of wrinkle peaks and troughs around the circumference at a maximum punch displacement of 75 mm.

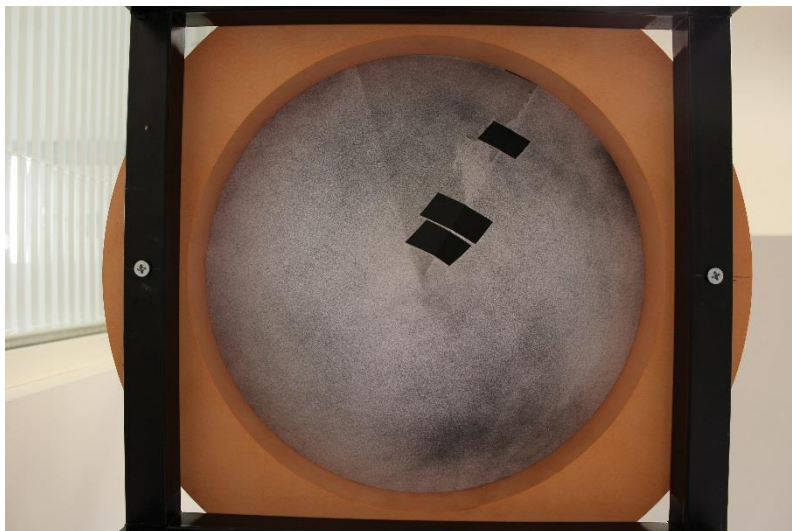


Figure A1. Typical image from the calibration cone. Black rectangles are adhesive tapes.

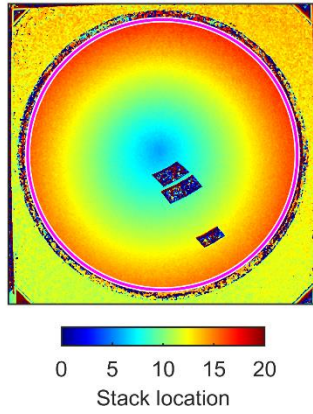


Figure A2. Raw height data for the calibration case, taken from the shape-from-focus analysis. The magenta circle marks the extent of the cone, located using the Hough transform algorithm.

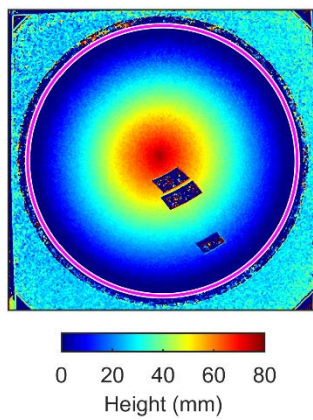


Figure A3. Scaled height data from the calibration case.

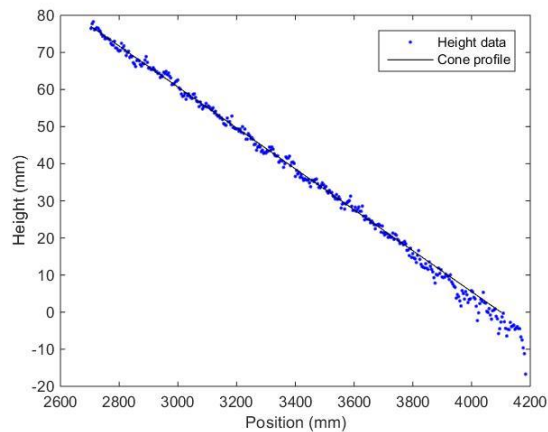


Figure A4. Variation in height data along a radius for the cone calibration case. The actual cone geometry is marked by the straight line.